Journal of Water Process Engineering 77 (2025) 108458

Contents lists available at ScienceDirect

Journal of Water Process Engineering

journal homepage: www.elsevier.com/locate/jwpe

Polyethyleneimine-assisted polydopamine co-deposition for fabricating loose reverse osmosis membranes with enhanced antifouling and selectivity for lithium extraction from geothermal brine

Pra Cipta Buana Wahyu Mustika [a,d], Richard Sudarmanto [d], Hansdersen Hermes Irawan [d,e], Ariel Halim Qiu [d], Putu Doddy Sutrisna [d], Sutijan Sutijan [a], Widi Astuti [b], Siti Nurul Aisyiyah Jenie [f], Khoiruddin Khoiruddin [g,h], Himawan Tri Bayu Murti Petrus [a,b,c,*]

[a] Chemical Engineering Department, Sustainable Mineral Metallurgical (SMMP), Faculty of Engineering, Universitas Gadjah Mada, Jl. Grafika No.2, Kampus UGM, Yogyakarta 55281, Indonesia
[b] Research Center for Mineral Technology, National Research and Innovation Agency (BRIN), Jl. Ir. Sutami Km. 15, Tanjung Bintang, Lampung Selatan 35361, Indonesia
[c] Unconventional Geo-Resources Research Center, Faculty of Engineering, UGM, Jl. Grafika No.2, Kampus UGM, Yogyakarta 55281, Indonesia
[d] Chemical Engineering Department, Faculty of Engineering, Universitas Surabaya, Jl. Raya Kalirungkut, Kampus UBAYA, Surabaya 60293, Indonesia
[e] Department of Chemical Engineering National Taiwan University of Science and Technology (Taiwan Tech), Keelung Rd., Da'an Dist., Taipei City 10607, Taiwan, ROC
[f] Research Centre of Chemistry, Research Organization of Nanotechnology and Materials, National Research and Innovation Agency (BRIN), Kawasan Sains dan Teknologi (KST) B. J. Habibie, Building 452, Serpong, Tangerang Selatan, Banten 15314, Indonesia
[g] Chemical Engineering Department, Institut Teknologi Bandung (ITB), Jl. Ganesa No. 10, Bandung 40132, Indonesia
[h] Research Center for Nanosciences and Nanotechnology, Institut Teknologi Bandung (ITB), Jl. Ganesa No. 10, Bandung 40132, Indonesia

ARTICLE INFO

Editor: Ludovic F. Dumée

Keywords:
Geothermal brine
PDA-PEI
Loose reverse osmosis
Antifouling
Nanofiltration

ABSTRACT

This study presents the fabrication and evaluation of a nanofiltration membrane modified with polydopamine–polyethyleneimine (PDA–PEI), designed to mimic the characteristics of a loose reverse osmosis (LRO) membrane. The membrane exhibits relatively lower water permeability while providing enhanced selective ion rejection, enabling the effective separation of monovalent ions such as lithium from sodium and potassium, along with efficient rejection of divalent ions like magnesium and calcium in geothermal brine. Surface modification significantly enhanced hydrophilicity, antifouling resistance, and monovalent–divalent ion selectivity. The optimal membrane (PDA:PEI = 1:1) demonstrated improved salt rejection and a high selectivity ratio ($SFLi^{+}/Mg^{2+} \approx 7.8$), with enhanced permeability (22.5 $L{\cdot}m^{-2}{\cdot}h^{-1}{\cdot}bar^{-1}$) and flux recovery (FRR up to 95.3 %) in real geothermal brine. Characterization revealed uniform surface morphology, decreased pore size, and increased negative charge and hydroxyl/amine functionalities that inhibited gypsum and silica scaling. These findings validate PDA – PEI modification as a robust strategy for advancing LRO membrane performance in lithium recovery from complex brines.

1. Introduction

Lithium, often referred to as "white gold," has become a crucial element in the global shift toward renewable energy, primarily due to its extensive use in lithium-ion batteries for electric vehicles and energy storage systems [1]. Lithium resources are predominantly found in three major geological formations: igneous rocks (25–35 %), sedimentary rocks (8–13 %), and brines (52–66 %), with brines serving as the most commercially significant source. Among these, geothermal brines present a promising alternative for lithium extraction due to their substantial lithium content and continuous replenishment.

Globally, a number of lithium–rich brine sources have been identified, each exhibiting distinct geochemical characteristics influenced by their geographical setting and geological history [2]. These variations, shaped by ongoing water – rock interactions, present challenges for achieving consistent extraction performance. Notable lithium-rich regions include the Salar de Atacama in Chile [3], recognized as one of the most significant global lithium brine deposits. In China, the saline lakes

* Corresponding author at: Chemical Engineering Department, Sustainable Mineral Metallurgical (SMMP), Faculty of Engineering, Universitas Gadjah Mada, Jl. Grafika No.2, Kampus UGM, Yogyakarta 55281, Indonesia.

https://doi.org/10.1016/j.jwpe.2025.108458
Received 19 June 2025; Received in revised form 31 July 2025; Accepted 31 July 2025

of Qinghai and Tibet also serve as important sources [4]. European geothermal sites such as those in the Upper Rhine Graben, spanning the French–German border, are increasingly gaining attention [5]. Similarly, the Salton Sea geothermal field in California is known for its exceptionally lithium-rich brines. The Lithium Triangle in South America–comprising Bolivia [6], Argentina, and Chile–hosts some of the world's most prominent lithium–bearing brine reservoirs [7], underscoring the strategic importance of this region in the global lithium supply chain.

Nanofiltration (NF) membranes have emerged as a promising technology for lithium extraction from brines, offering advantages such as high energy efficiency, operational simplicity, and superior ion selectivity [8]. A key benefit of NF is its ability to effectively separate lithium from magnesium in brines with high Mg/Li ratios, a challenge that conventional extraction methods struggle to address. Unlike traditional evaporation ponds, NF significantly reduces water loss and environmental impact, making it a more sustainable option [9,10]. Additionally, NF provides higher separation efficiency with lower chemical consumption compared to solvent extraction and precipitation techniques, enhancing its feasibility for large-scale applications [11,12].

In recent years, LRO membranes have gained attention as an alternative separation technology due to their ability to operate at lower pressures than conventional RO, thereby reducing energy consumption while maintaining effective ion separation [13]. LRO membranes offer high rejection toward divalent ions such as Mg^{2+} and Ca^{2+}, and moderate rejection of monovalent ions like Na^{+} and K^{+}, while allowing relatively higher permeability of Li^{+}. This selective ion transport behavior makes LRO membranes particularly suitable for lithium extraction from brine solutions.

Despite the advantages of NF and LRO membranes, fouling and scaling remain significant challenges in their application for lithium extraction from brines. Organic fouling, primarily caused by the deposition of polysaccharides, proteins, and humic substances, forms dense layers on the membrane surface, reducing permeability and efficiency [14,15]. Inorganic scaling, dominated by calcium carbonate ($CaCO_3$), calcium sulfate ($CaSO_4$), and magnesium salts, leads to crystalline deposition that clogs membrane pores and impairs separation performance [14,16,17]. The high salinity and complex ionic composition of brines, particularly those with elevated Mg/Li ratios, exacerbate fouling by promoting competitive ion interactions and the precipitation of sparingly soluble salts [16]. Additionally, biofouling caused by microbial growth contributes to membrane clogging and structural degradation, further diminishing lithium recovery efficiency [18]. These persistent fouling issues necessitate frequent membrane cleaning and replacement, underscoring the need for antifouling modifications and effective pretreatment strategies.

To address these challenges, surface modification strategies have been explored to enhance membrane performance. Membrane surface modification by increasing hydrophilicity, smoothing surface roughness, and regulating surface charge can significantly improve antifouling performance [19,20]. Hydrophilic and smooth surfaces reduce foulant adhesion, while introducing negative or zwitterionic charges enhances electrostatic repulsion against charged contaminants [21]. Various approaches, including grafting hydrophilic polymers, incorporating zwitterionic or charged groups, and embedding nanomaterials, have demonstrated improvements in membrane performance by reducing foulant adhesion and enhancing surface hydrophilicity [22–24].

Among these, PDA modification stands out as a highly promising and scalable solution due to its bioinspired adhesion properties, ease of deposition, and ability to serve as a versatile platform for further functionalization [25,26]. PDA coatings significantly improve membrane hydrophilicity, imparting a negative surface charge that mitigates organic fouling while also exhibiting inherent antibacterial properties through protonated amine groups [27]. Furthermore, PDA modifications can be industrially scaled and applied under mild conditions, making them a cost-effective and efficient choice for improving antifouling resistance in NF and RO membranes [28,29].

The incorporation of a PDA/PEI interlayer in NF membranes resulted in a twofold increase in water permeation flux while maintaining a high Na_2SO_4 rejection of 97 % [30]. Similarly, a PDA-based interlayer in thin-film nanocomposite NF membranes enhanced water permeance nearly tenfold, from 2.4 to 14.8 $L/m^2{\cdot}h{\cdot}bar$, optimizing separation performance while preserving salt rejection [31]. Additionally, pressure-assisted PDA modification of thin-film composite (TFC) RO membranes resulted in an increase in water permeance to 3.31 LMH/bar while achieving a high salt rejection of 98.95 % [32].

The antifouling properties of PDA – modified membranes have been extensively demonstrated, with a PDA – based three – layer architecture achieving a flux recovery rate above 96 % [33]. The modification of NF membranes using PDA/PEI resulted in an exceptionally high-water flux of 26.2 $L{\cdot}m^{-2}{\cdot}h^{-1}{\cdot}bar^{-1}$, while maintaining low Na_2SO_4 rejection (5.1 %), enabling effective monovalent-divalent ion separation [34]. Furthermore, studies comparing slow and fast dopamine polymerization processes revealed that PDA – coated membranes consistently exhibited NaCl rejection above 93 %, with membranes possessing a lower number of PDA layers demonstrating superior NaCl rejection (94 %) compared to unmodified XLE membranes [35].

This study aims to systematically evaluate the performance consistency of PDA–PEI modified NF membranes, designed to mimic the characteristics of LRO membranes, in the context of lithium extraction from geothermal brine. The research will comprehensively assess both pristine and modified membranes in terms of water flux, ion rejection, selectivity, and operational stability, particularly their ability to sustain flux over prolonged operation. By conducting a detailed performance analysis, this study seeks to provide a deeper understanding of the reliability and effectiveness of PDA–PEI modification, contributing to the optimization of membrane-based lithium recovery processes.

2. Materials and methods

2.1. Materials

A thin–film composite (TFC) nanofiltration membrane (NF3) was procured from RisingSun Membrane Technology (Beijing) Co., Ltd., and, according to the manufacturer's specifications, is equivalent to the NF270 membrane from Dow FilmTec™ (https://www.risingsunmembranes.com). According to Guo et al., the NF270 membrane consists of a polyamide (PA) active layer supported by polysulfone (PSf), a structure also identified by Lim et al. in the NF3 membrane. This similarity is supported by comparable functional group characteristics, and separation performance, particularly their low rejection of monovalent ions such as Na^{+} (19.4 % for NF270 and ~16.3 % for NF3) [36,37]. Under identical test conditions using a 2000 ppm $MgSO_4$ solution, the manufacturers report that both the NF270 (https://www.dupont.com) and NF3 membranes exhibit high rejection of divalent ions (Mg^{2+}), with values equal to or exceeding 97 %.

All chemicals used in this study were of analytical grade and did not require further purification. The modifying agents, including (1) dopamine hydrochloride, (2) branched polyethyleneimine, (3) Trizma® hydrochloride, and (4) sodium hydroxide (NaOH), were obtained from Sigma–Aldrich. Ultrapure water, used in the membrane modification process, was purchased from OneMed under the trade name WaterOne, while the pure water used for preparing the geothermal brine solution was produced in-house using a RO system in the laboratory, with a maximum conductivity of 15 μS/cm.

The synthetic geothermal brine was prepared using a mixture of salts, all purchased from Sigma-Aldrich, including (1) lithium chloride (LiCl), (2) sodium chloride (NaCl), (3) potassium chloride (KCl), (4) calcium chloride ($CaCl_2$), (5) magnesium sulfate ($MgSO_4$), (6) magnesium chloride ($MgCl_2$), calcium sulfate ($CaSO_4$), and (7) sodium silicate (Na_2SiO_3). Additionally, non-ionic compounds were used for membrane pore size measurements, including (1) xylose, (2) glucose, (3) dextrose,

and (4) sucrose.

2.2. Membrane preparation

TFC NF3 membrane was first rinsed with deionized water to eliminate residual preservatives, followed by thorough washing with ultrapure water. To ensure complete hydration and surface stabilization, the membranes were subsequently immersed in ultrapure water for 24 h prior to the modification process. For surface modification, dopamine hydrochloride (1 g/L) and branched PEI were dissolved in a Trizma® hydrochloride buffer solution (pH 8.5), with pH adjustments made using 0.1 N NaOH as needed. Three different dopamine–to–PEI mass ratios: 1:0, 1:1, and 1:2 were formulated to investigate the influence of composition on membrane performance. These conditions are referred to as M1, M2, and M3, respectively.

Each NF3 membrane was cut into standardized dimensions (7 cm × 12 cm), and 120 mL of the corresponding modification solution was used per sample. The membranes were fully immersed in the solution to ensure uniform surface contact, and the co-deposition reaction was carried out under mild agitation at 60 rpm for 2 h. Post–modification, the membranes were thoroughly rinsed with ultrapure water to remove unreacted monomers and by-products. They were then air-dried for 24 h to promote complete polymerization and stabilization of the coating layer. Prior to performance testing, the membranes were rehydrated by immersion in ultrapure water for another 24 h. A schematic overview of the membrane modification procedure is presented in Fig. 1, followed by a detailed comparison of the pristine and modified membranes in Fig. 2.

2.3. Membrane characterization

The surface chemical composition of the membranes was characterized using Fourier Transform Infrared Spectroscopy (FTIR) [Shimadzu, IRTracer-100] over a spectral range of 500–4500 cm^{-1}, enabling the identification of functional groups and verification of chemical modifications resulting from the PDA-PEI coating. Surface morphology and structural features were examined using Scanning Electron Microscopy (SEM) [Zeiss EVO MA10 and Thermo Scientific Quattro S], providing high–resolution imaging to evaluate surface texture, roughness, and coating uniformity. To complement the SEM analysis, surface topography was further characterized by Atomic Force Microscopy (AFM) [Nanosurf, FlexAFM], offering nanoscale insights into surface roughness and spatial distribution. The membrane's hydrophilicity was quantified by contact angle measurements using a goniometer [Krüss, D5A255], which allowed for precise evaluation of wettability and changes in surface energy following surface modification.

2.4. Membranes performed test

The separation efficiency and fouling resistance of the membranes prior to and following surface modification were systematically assessed using a bench–scale cross–flow (CF042) filtration unit operated at 7–8 bar and maintained at a constant temperature of approximately 37 °C. A schematic of the experimental setup is shown in Fig. 3. The assessment consisted of three investigative stages to comprehensively examine the membrane's rejection efficiency, ion selectivity, and long-term operational stability under simulated geothermal brine conditions.

The first stage investigation focused on single-ion solutions to analyze the baseline separation performance of the membranes. The tested solutions included LiCl at concentrations of 200, 250, and 300 mg/L; NaCl–KCl at 4400, 6000, and 7500 mg/L; and $CaCl_2$–$MgSO_4$ at 600, 750, and 900 mg/L.

The second stage investigation examined binary–ion solutions to assess the membrane's ion selectivity. The tested ion pairs included (1) Li^+/Mg^{2+}, (2) Li^+/Ca^{2+}, (3) Na^+/Mg^{2+}, and (4) Na^+/Ca^{2+}, (5) K^+/Mg^{2+}, (6) K^+/Ca^{2+} providing insights into the preferential separation of lithium over competing cations. The third stage investigation simulated long–term operational consistency under conditions resembling real geothermal brine environments. This evaluation involved four test scenarios: (1) multi-ion solution with gypsum, (2) multi–ion solution with silica, (3) multi–ion solution containing both gypsum and silica (SGB), and (4) real geothermal brine (RGB) [38]. Each scenario aimed to assess the membrane's stability, fouling resistance, and sustained performance in complex feed compositions. Detailed compositional information is provided in Table S2, while a schematic representation of the research methodology is shown in Fig. S1.

Throughout all experimental stages, the pH was maintained at approximately 6.8 to ensure controlled and comparable testing conditions. Membrane performance was quantitatively evaluated by calculating permeability (L_P), flux recovery ratio (FRR), rejection (R), and selectivity (SF) using Eqs. (1), (2), (3), and (4), respectively, to determine ion separation efficiency and overall filtration effectiveness.

$$L_P = \frac{V}{A \times \Delta t \times TMP} \quad (1)$$

where V, A, Δt, and TMP represent the permeate volume (L), active membrane area (m^2), data collection time (h), and transmembrane pressure (bar), respectively. The reduction in membrane permeability was observed, indicating a decline in the membrane's ability to transport permeate. This decrease was quantitatively assessed using Eq. (2) to evaluate changes in flux performance [31].

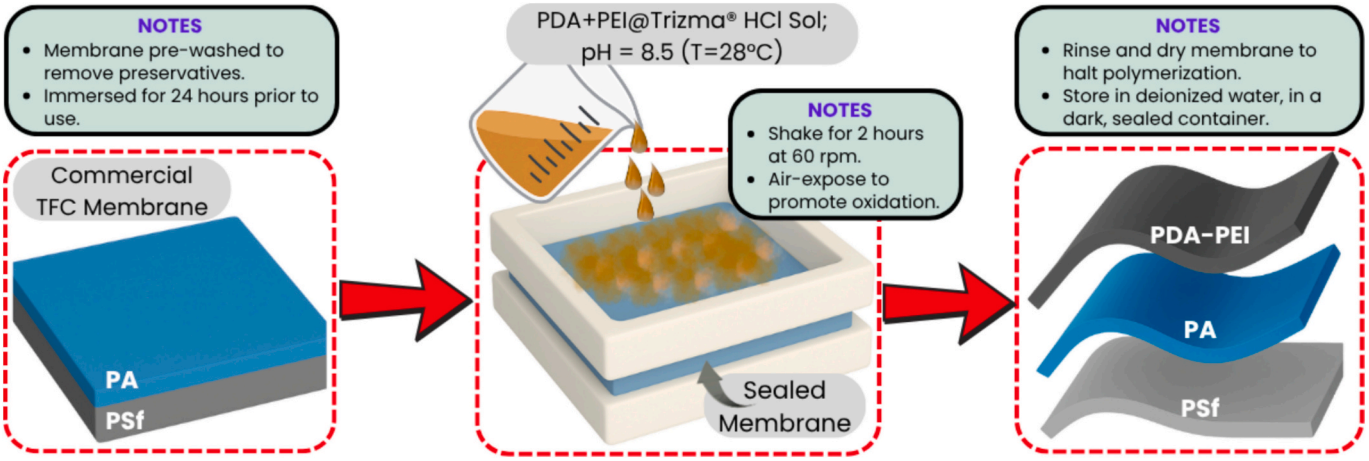

Fig. 1. Schematic illustration of the stepwise modification of nanofiltration (NF) membranes using PDA-PEI co-deposition.

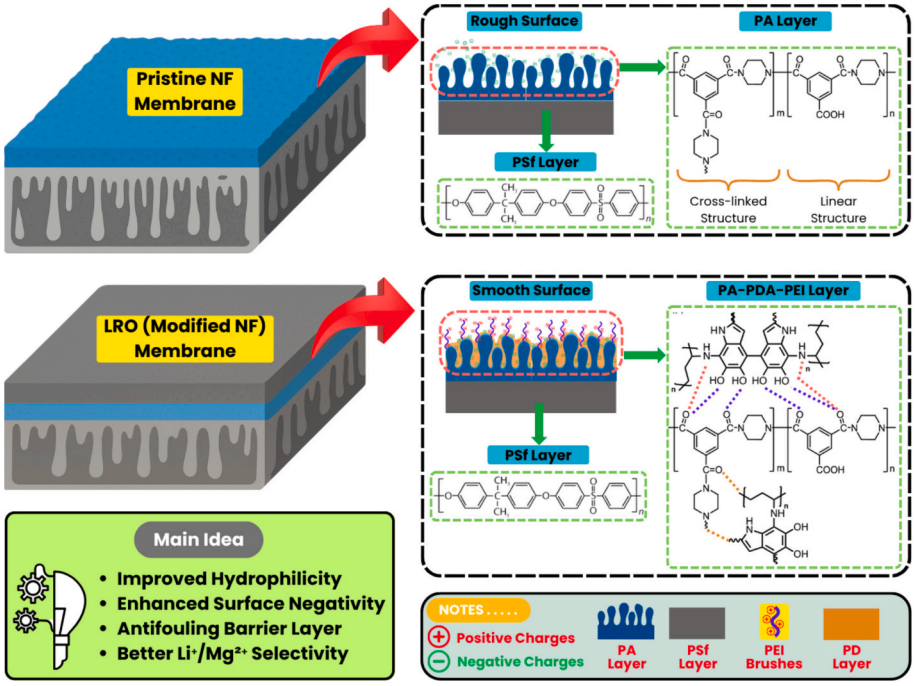

Fig. 2. Comparison of expected characteristics between pristine NF membranes and modified loose reverse osmosis (LRO) membranes.

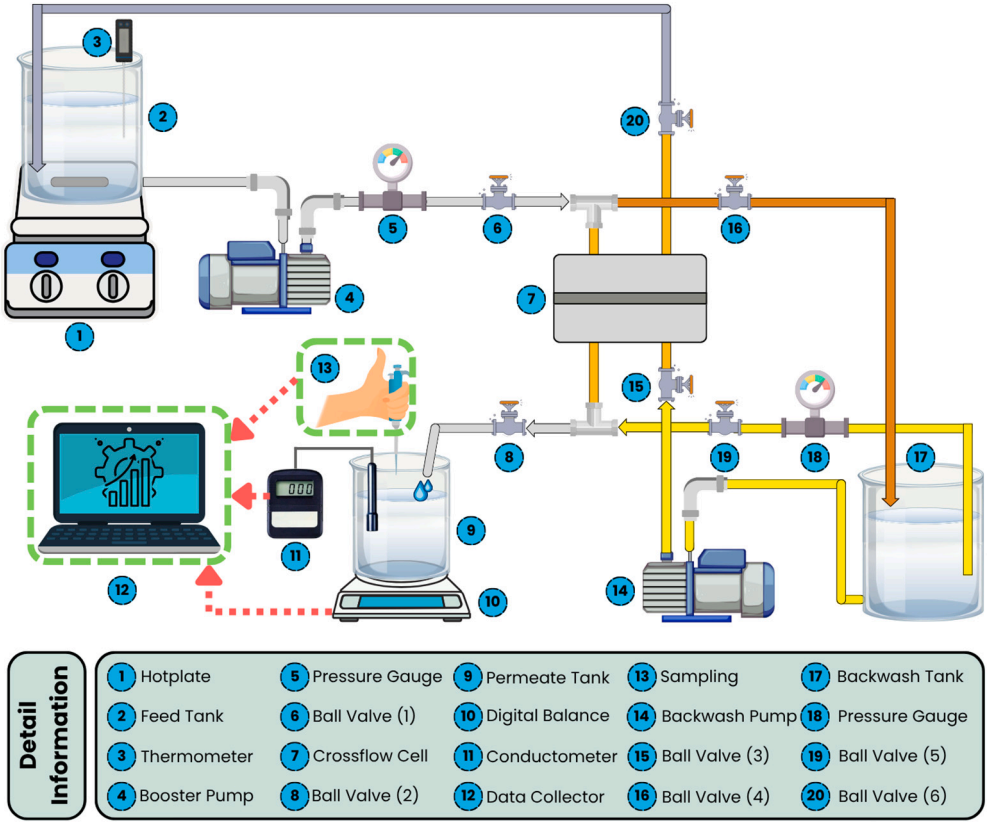

Fig. 3. Schematic diagram of the loose reverse osmosis (LRO) system setup.

$$FRR\% = \left(1 - \frac{L_{p,i}}{L_{p,f}}\right) \times 100\% \quad (2)$$

where $L_{p,i}$ represents the initial membrane permeability, and $L_{P,t}$ denotes the permeability at a final time [t]. Rejection quantifies the membrane's efficiency in preventing ions from passing through during filtration.

$$R\% = \left(1 - \frac{C_P}{C_F}\right) \times 100\% \quad (3)$$

where C_P and C_F represent the permeate concentration (mg/L) and feed concentration (mg/L), respectively. Selectivity characterizes the membrane's ability to differentiate and separate specific ions [8].

$$SF = \frac{C_{N,P}/C_{M,P}}{C_{N,F}/C_{M,F}} \quad (4)$$

where $C_{N,P}$ and $C_{M,P}$ represent the concentrations of the target ions in the permeate, while $C_{N,F}$ and $C_{M,F}$ correspond to their respective concentrations in the feed solution.

2.5. Membrane molecular weight cut–off (MWCO) and pore size distribution

The molecular weight cut–off (MWCO) performance of the LRO membrane was evaluated by filtering a 1000 ppm solution of various neutral organic molecules (NOM) with known molecular weights: xylose (150.1 Da), glucose (180 Da), dextrose (198 Da), and sucrose (342 Da), each under an applied pressure of 5 bar. The MWCO of the membrane is defined as the molecular weight corresponding to 90 % solute rejection. To facilitate determining the molecular weight value, the approximation line used is the asymptotic regression model–1st parameterization available in the OriginPro®2024 software. The Stokes radius MWCO (r_s) of the membrane was calculated using Eq. (5).

$$r_S = 35.788 \times 10^2 \times MWCO^{43.762\times10^2} \quad (5)$$

Solute concentrations in the feed and permeate were determined using High-Performance Liquid Chromatography (HPLC) [Agilent, 1260 Infinity II]. Pore size distribution was then analyzed using a probability density function, as described by Eq. (6) [29].

$$\frac{dR(r_P)}{dr_P} = \frac{1}{r_P \ln\sigma_P \sqrt{2\pi}} \exp\left(\frac{-(\ln r_P - \ln\mu_P)}{2(\ln\mu_P)^2}\right) \quad (6)$$

The average effective pore size of the membrane (μ_P) is defined as the Stokes radius corresponding to 50 % rejection of the neutral organic molecules (NOM). The geometric standard deviation (σ_P) of the membrane pore size distribution is determined from the ratio of the Stokes radii at 84.1 % and 50 % rejection, respectively.

3. Results and discussion

3.1. Membrane characterizations

NF3 membrane modification of a via PDA–PEI copolymerization was successfully conducted. The effectiveness of the membrane modification is primarily evaluated based on two critical performance parameters: separation efficiency and antifouling capability. However, a deeper understanding of the modification mechanism requires comprehensive membrane characterization, including: (1) surface morphology and topography, (2) chemical composition, (3) hydrophilicity, and (4) pore structure.

SEM analysis was performed to investigate changes in surface morphology, as shown in Fig. 4A. M0 exhibited a smooth and defect-free surface with uniform morphology. In contrast, M1–M3 demonstrated increasingly irregular surface textures, suggesting the influence of PDA–PEI deposition on surface characteristics. For membrane M1, surface modification using PDA alone led to the appearance of noticeable

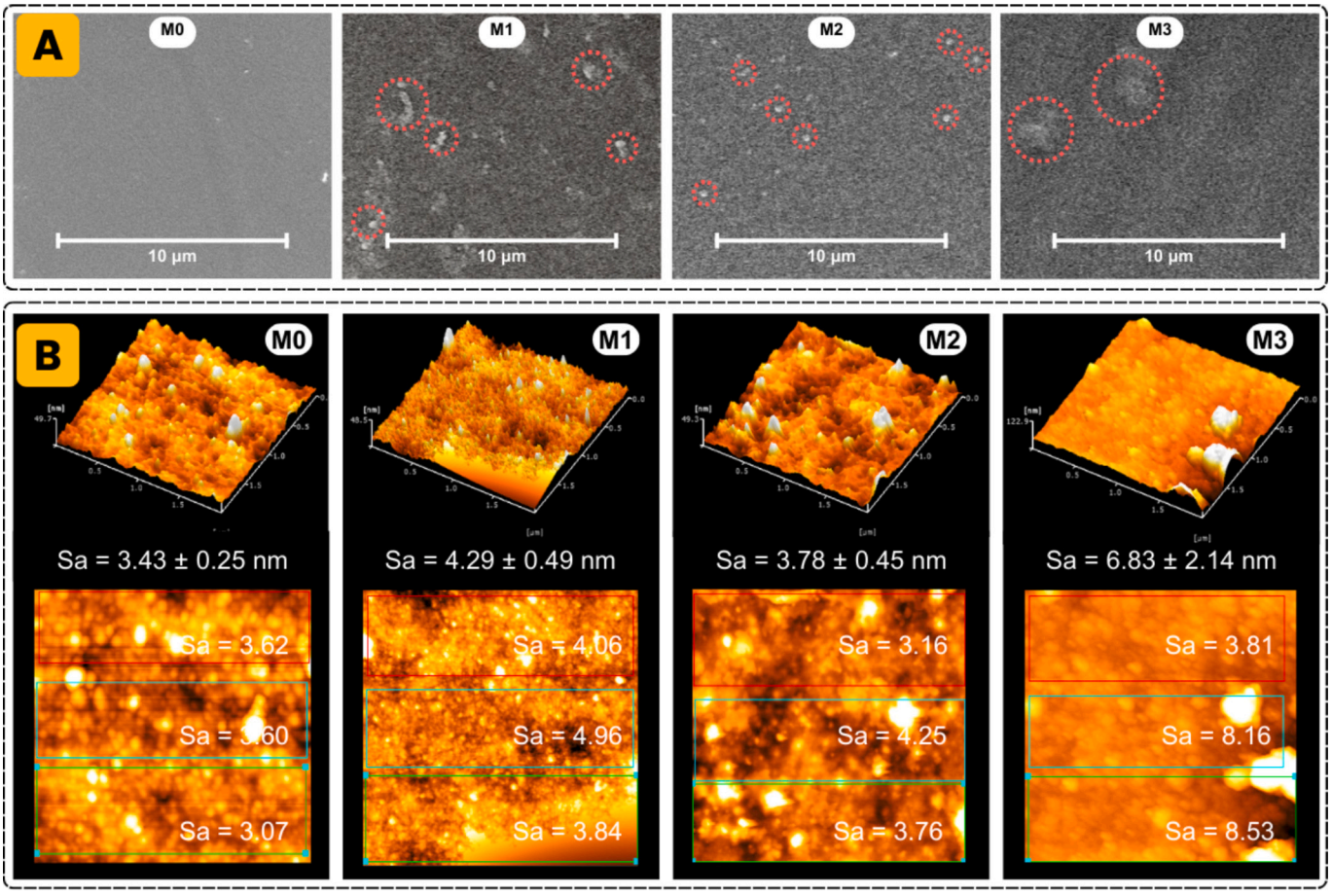

Fig. 4. SEM and AFM topographical analysis of membrane surfaces: M0 (Pristine membrane), M1 (PDA:PEI = 1:0), M2 (PDA:PEI = 1:1), and M3 (PDA:PEI = 1:2). The images illustrate surface morphology variations due to PDA-PEI modifications, highlighting changes in roughness, aggregation, and coating uniformity.

particulate aggregates. While PDA is theoretically intended to smooth the surface by forming a uniform coating, the self-polymerization of dopamine often causes aggregation, resulting in non–uniform layer thickness. This effect is evident in the M1 membrane, which shows increased surface roughness compared to the pristine M0 membrane.

The introduction of PEI through copolymerization with PDA (observed in M2) was effective in mitigating excessive PDA aggregation [39]. This improvement is attributed to the ability of PEI to form covalent bonds with dopamine via Michael addition or Schiff base reactions between PEI's amine groups and PDA's catechol moieties, facilitating a more uniform and homogeneous deposition layer on the membrane surface [40–42]. Nevertheless, excessive incorporation of PEI, as seen in M3, led to the re-emergence of large agglomerates, likely due to over-saturation and uneven polymeric network formation [40,43]. This suggests that an optimal ratio of PDA to PEI is crucial for achieving a well-controlled and uniform surface structure.

To complement the SEM analysis, AFM was employed to quantitatively assess membrane surface roughness at the nanoscale. AFM offers high-resolution topographical data, enabling precise evaluation of the impact of PDA and PDA–PEI copolymer coatings on surface morphology (Fig. 4B–C). M0 exhibited an average roughness (Sa) of 3.43 ± 0.25 nm, with a consistent topographic profile across the scanned area (Sa range: 3.07–3.62 nm). Upon PDA modification (M1), surface roughness increased to an average Sa of 4.25 ± 0.49 nm (range: 3.84–4.96 nm), indicating the formation of a non–uniform PDA layer that slightly changed the surface texture, this is in accordance with the information from the SEM images previously mentioned.

Further modification with PEI copolymer showed variable effects depending on its concentration. In M2, where an optimal PEI amount was applied, the surface roughness slightly decreased to Sa = 3.78 ± 0.45 nm (range: 3.16–4.25 nm), suggesting a mild reorganization of the surface structure due to co–deposition. Despite this decrease, the surface remained smooth and homogenous. In contrast, excessive PEI addition in M3 led to a significant increase in surface roughness, with an average Sa of 6.83 ± 2.14 nm and a broader range of 3.81–8.53 nm, indicating pronounced surface heterogeneity and irregularities. This phenomenon can be attributed to the high concentration of amine groups introduced under excessive PEI conditions, which results in an overabundance of reactive sites. Such conditions promote surface oversaturation and disrupt the reaction equilibrium between oxidized dopamine (quinone) and amine groups, ultimately leading to the formation of an uneven polymeric network. Consequently, uncontrolled layer growth promotes macro-scale aggregation, and instead of forming a uniform coating, excessive PEI induces structural irregularities and aggregate formation, thereby increasing surface roughness [44].

Similar observations regarding changes in membrane surface roughness due to PDA and PEI modification have been reported in the literature. For instance, Li et al. demonstrated that surface coating of a reverse osmosis polyamide (RO–PA) membrane with PDA, followed by PEI grafting, led to an increase in root mean square (RMS) roughness

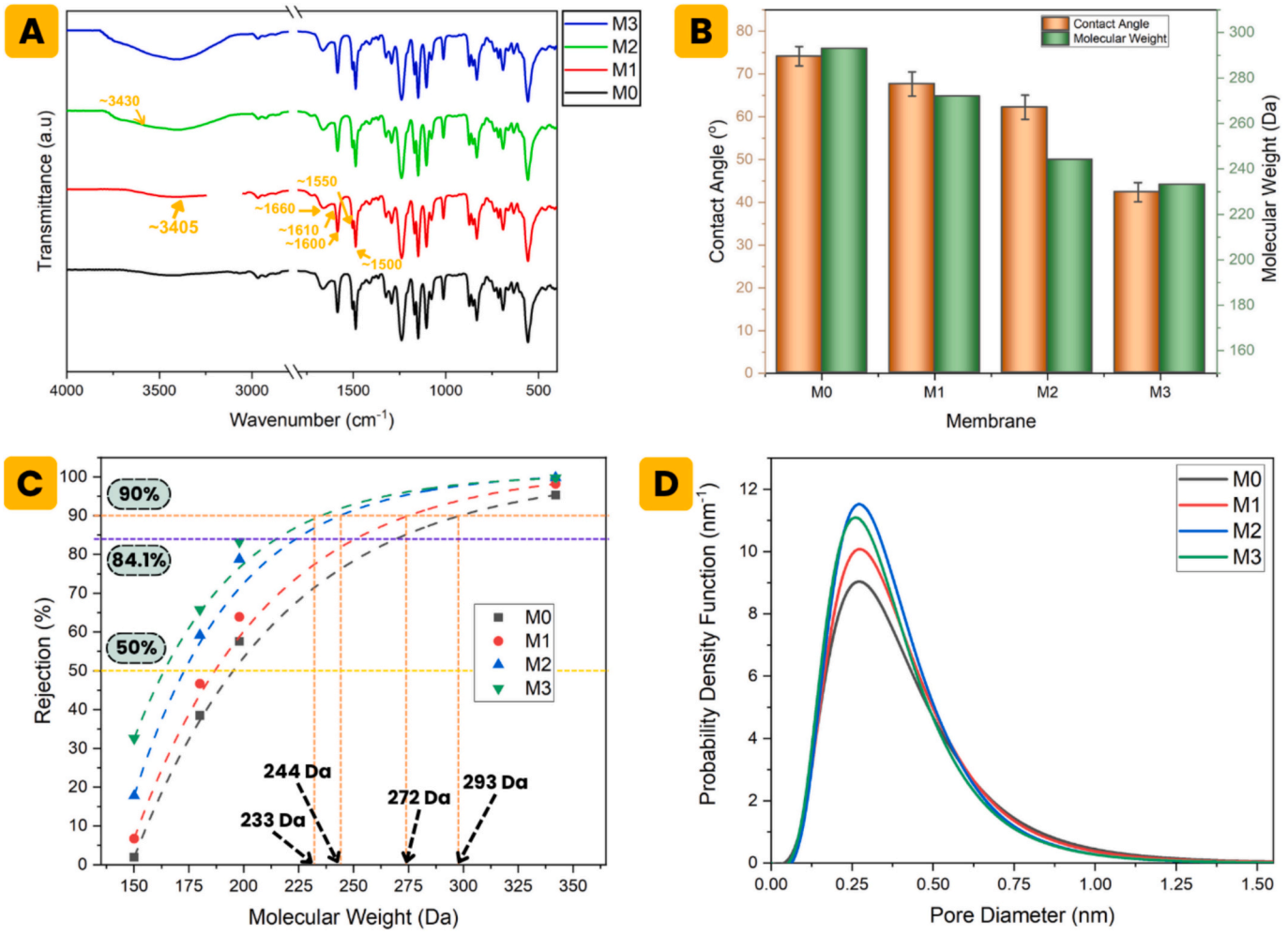

Fig. 5. (A) FTIR spectra of the pristine membrane (M0) and modified membranes (M1–M3), illustrating chemical functional group changes upon surface modification. (B) Comparison of contact angle and molecular weight cut-off (MWCO) for M0 and M1–M3, highlighting variations in surface wettability and morphological characteristics.

from 60.97 nm to 79.51 nm, indicating the formation of a more textured surface [45]. Likewise, Ashraf et al. observed an increase in RMS roughness from 9.6 nm to 13.1 nm upon PDA-PEI modification of a nanofiltration polyamide (NF–PA) membrane [46]. This suggests that an overabundance of PEI leads to inhomogeneous co–deposition, resulting in uneven surface layering and the formation of large aggregates. These findings are consistent with SEM results, confirming that excessive PEI disrupts uniform film formation and leads to surface heterogeneity.

Chemical modifications introduced by PDA and PEI are evident from the changes in functional group characteristics, as depicted in the FTIR spectra (Fig. 5A). M0 exhibits characteristic peaks at 1660, 1600, and 1550 cm^{-1}, corresponding to C═O stretching, hydrogen-bonded C═O, and in-plane N—H bending vibrations, respectively, which originate from the PA layer. Similarly, Eltahan et al. identified PA–specific peaks at 1698 cm^{-1} (amide I), 1549 cm^{-1} (amide II), and additional bands at 1250 cm^{-1} (amide III), as well as 1610 and 1489 cm^{-1} corresponding to aromatic ring vibrations, further confirming the presence of the PA active layer on TFC membranes [47]. Following modification (M1–M3), a reduction in peak intensities at 1660 and 1600 cm^{-1} is observed. This decrease can be attributed to the oxidation of catechol dopamine into dopamine quinone during the polymerization process [48]. Additionally, a broadening of the absorption band at ~3430 cm^{-1} is evident, likely due to increased hydrogen bonding within the polymerized PDA network. These spectral changes confirm successful PDA deposition and the associated chemical transformations induced by dopamine oxidation and cross-linking with PEI [46,49].

The hydrophilic nature of the modified membranes is primarily governed by the presence of hydroxyl, carboxyl, and amine functional groups within the PDA layer, which inherently enhance surface hydrophilicity [50]. As evidenced by water contact angle measurements (Fig. 5B), an increase in hydrophilicity is observed following PDA–PEI modification. M0 exhibits a contact angle of 74.15 ± 2.27°, reflecting its relatively low hydrophilicity. Upon surface modification, a progressive decrease in contact angle is observed: 67.67 ± 2.82° for M1 (PDA only), 62.23 ± 2.28° for M2, and 42.35 ± 2.25° for M3 (PDA/PEI), indicating enhanced surface hydrophilicity. This reduction is primarily attributed to the incorporation of hydrophilic functional groups introduced through the deposition of PDA and PDA/PEI layers. The application of PDA alone results in a modest improvement, with a decrease of less than 10°, while the co–deposition with PEI yields a more significant reduction. PEI serves not only as a source of additional amine groups but also as a polymerization regulator, facilitating more controlled deposition and improved surface morphology [51].

The PDA–PEI modification plays a critical yet indirect role in regulating the effective pore radius (r_P) of the LRO membrane, a parameter closely linked to the membrane's separation performance. As illustrated in Fig. 5B, both the self–polymerization of PDA and its co–polymerization with PEI consistently result in a reduction of the membrane's pore radius. This trade–off reflects a key aspect of membrane design, where increased selectivity often comes at the cost of reduced permeability.

As detailed in Section 2.5, the pore radius in this study was not measured directly, but rather estimated by correlating it with MWCO at 90 % rejection of neutral organic molecules (NOM), as shown in Fig. 5C. M0 exhibited an MWCO of 293 Da. Upon modification with PDA alone (M1), the MWCO decreased to 272 Da, indicating a moderate reduction in pore size. Interestingly, while PEI is often introduced to control polymerization and maintain structural uniformity, its incorporation in this study (membranes M2 and M3) led to further reductions in MWCO values to 244 Da and 233 Da, respectively.

This suggests that, despite PEI's role as a polymerization regulator minimizing excessive pore clogging and stabilizing the surface layer [32], its presence may still contribute to tighter pore structures under certain conditions. The resulting diversity in pore size distributions was further analyzed using probability density functions, as depicted in Fig. 5D. The modified membranes displayed a denser distribution of pore radii, predominantly centered around ~0.25 nm, indicating a more compact and selective membrane structure. This pore structure refinement is largely enabled by the self-polymerization of PDA and its enhanced organization via PEI copolymerization.

However, it is important to note that excessive polymerization either due to prolonged reaction time or rapid aggregation may lead to non-uniform particle deposition, adversely affecting the consistency of pore size. A similar phenomenon was reported by Yu et al., who investigated PDA/PEI modifications on PES–based membranes for Li^+/Mg^{2+} separation [52]. In that context, the PDA and PEI layers formed stable interactions with the underlying PA layer through covalent bonding, π–π stacking, and other non-covalent interactions, further contributing to membrane stability and functional performance [53].

3.2. Membrane efficiency and fouling resistance to

Membrane performance evaluations were conducted following the procedure outlined in Section 2.4. Initially, a systematic assessment of M0 was performed, focusing on the stability of both water and salt permeability, as illustrated in Figs. S3 and S4. The permeate flux profile in Fig. S3 indicates that M0 consistently maintains stable water transport across various feed concentrations, confirming its operational reliability under fluctuating solution compositions. Correspondingly, the salt permeability data in Fig. S4 show consistent salt transport behavior, suggesting a proportional relationship between salts and water permeability. This consistency implies that the membrane's separation mechanism is primarily governed by a balance between convective and diffusive transport processes. Additionally, the pristine membrane exhibited a pure water permeability (PWP) of 20.48 ± 0.52 $L{\cdot}m^{-2}{\cdot}h^{-1}{\cdot}bar^{-1}$, reflecting its inherent hydraulic permeability.

The single-ion rejection analysis revealed a clear distinction in separation performance between monovalent and divalent cations for M0. As shown in Fig. S3, M0 exhibited relatively low and variable rejection efficiencies for monovalent ions, with rejection values ranging from 2.36 to 3.33 % for Li^+, 2.44–4.33 % for Na^+, and 3.60–4.55 % for K^+. In contrast, significantly higher and more stable rejection was observed for divalent cations, with Ca^{2+} at 44.01–52.76 % and Mg^{2+} at 87.51–89.66 %. These trends are consistent with the findings of Li et al., who reported the rejection order as $RLi^+ < RNa^+ < RK^+ < RCa^{2+} < RMg^{2+}$ [54]. This selective rejection behavior is primarily governed by size exclusion and electrostatic interactions. The pristine membrane's effective pore radius, as previously correlated with an MWCO of ~293 Da (~0.36 nm), serves as a physical barrier that favors the rejection of larger or more highly hydrated ions. According to data reported by Tansel et al., the hydration radii of Li^+, Na^+, and K^+ are approximately 0.340–0.382 nm, 0.276–0.360 nm, and 0.201–0.331 nm, respectively. Meanwhile, divalent ions exhibit larger hydration shells, with Ca^{2+} ranging from 0.412 to 0.420 nm and Mg^{2+} from 0.300 to 0.470 nm [55]. The relatively low rejection of monovalent ions can be attributed to their smaller hydration radii and weaker electrostatic interactions with the membrane surface, allowing them to diffuse more readily through membrane pores [56]. Furthermore, the variability in monovalent ion rejection suggests greater sensitivity to feed concentration and ionic strength. In contrast, the consistent rejection of divalent ions is likely due to their larger hydrated size and stronger charge-based interactions, resulting in more predictable exclusion behavior [57,58].

From the perspective of lithium extraction, the current membrane performance is highly promising. Nevertheless, when applied to brines with complex compositions and high levels of contaminants, fouling resistance becomes a critical factor. To address this, the incorporation of PDA–PEI is anticipated to enhance the antifouling properties of the membrane.

A comparative overview of ion rejection by both pristine and modified membranes is presented in Fig. 6A (Stage 1). The pristine membrane demonstrated moderate rejection toward divalent salts, with $MgSO_4$ and $CaCl_2$ rejection values of 87.5 ± 3.1 % and 52.8 ± 2.7 %,

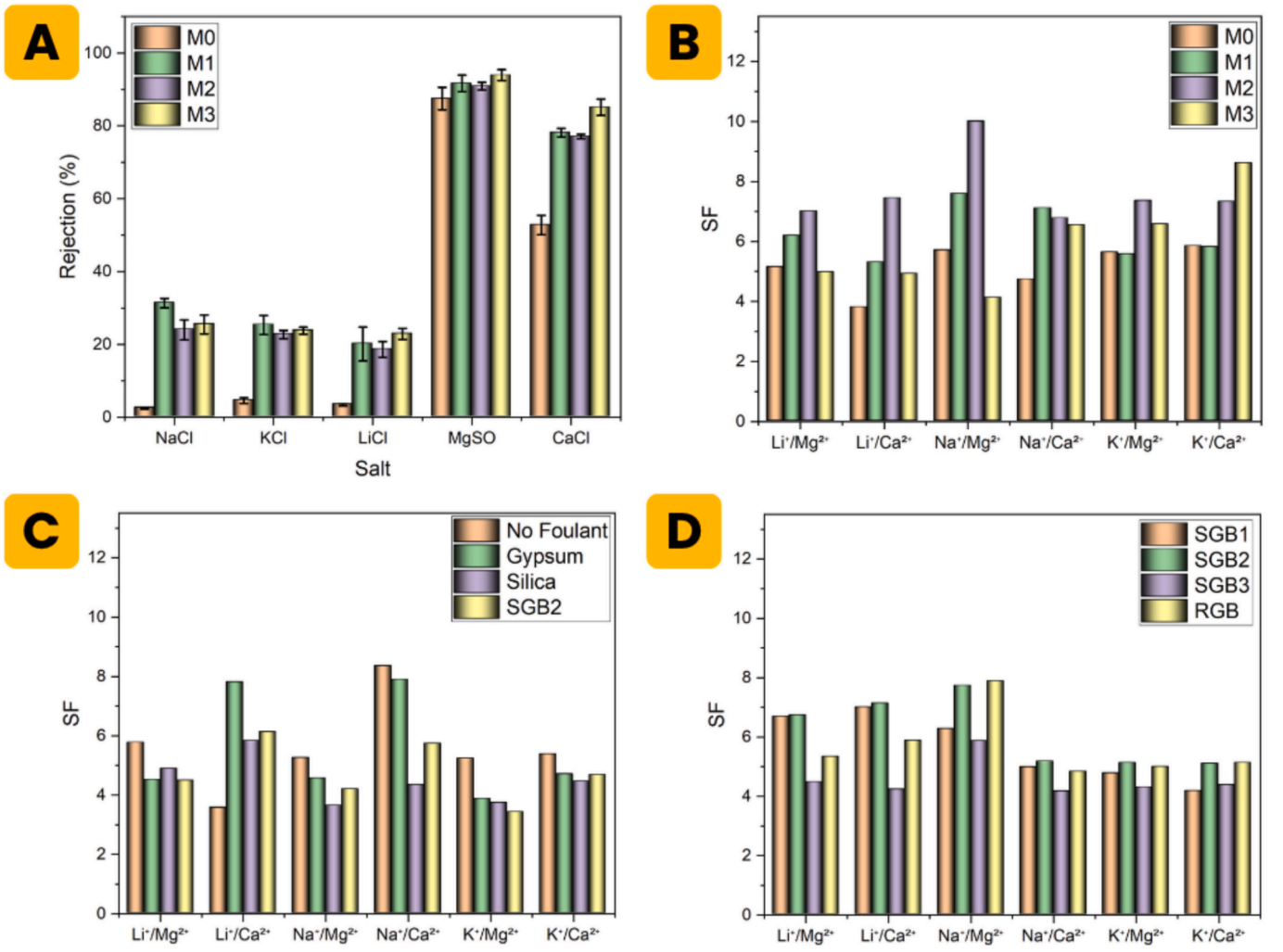

Fig. 6. Comprehensive performance evaluation of pristine (M0) and PDA–PEI modified membranes (M1–M3): (a) rejection of various individual salts, (b) ion selectivity between monovalent and divalent salt pairs; (c) effect of different foulants (silica, gypsum, and their combination) on the ion selectivity of M0; and (d) monovalent/divalent ion selectivity of M2 in simulated and real geothermal brine environments.

respectively. Upon surface modification with PDA and PEI, a progressive enhancement in salt rejection was observed. For $MgSO_4$, rejection improved slightly across the modified membranes, reaching 91.7 ± 2.3 % for M1 (PDA-only), 90.9 ± 1.1 % for M2 (PDA:PEI = 1:1), and 93.9 ± 1.5 % for M3 (PDA:PEI = 1:2). Similarly, the rejection of $CaCl_2$ increased more markedly, particularly for M3, which achieved a rejection of 85.1 ± 2.2 %.

These improvements can be attributed to enhanced surface hydrophilicity and the introduction of functional groups through the PDA–PEI co–deposition [59]. The catechol and amine functionalities in PDA and PEI respectively can form a denser and more hydrated surface layer, leading to a greater steric hindrance and Donnan exclusion effect, which is more pronounced for divalent ions such as Ca^{2+} and Mg^{2+} [46,60].

Interestingly, a more substantial increase was observed in the rejection of monovalent salts (LiCl, NaCl, and KCl), which originally exhibited low rejection by M0. For instance, LiCl rejection increased from 3.4 ± 0.3 % in M0 to 22.8 ± 1.5 % in M3. Similarly, NaCl rejection rose from 2.4 ± 0.2 % to 31.3 ± 1.3 % in M1 and remained above 23 % in M2 and M3. A comparable trend was observed for KCl. This notable enhancement is likely due to the increase in surface charge density induced by PEI incorporation. The presence of multiple amine groups in PEI introduces a higher density of positively charged sites [45,61], especially under neutral pH, which repels co–ions (e.g., Cl^-), thereby enhancing ion rejection, particularly for monovalent salts that previously exhibited minimal interaction with the membrane.

In terms of ion selectivity (see Fig. 6B), the pristine membrane displayed relatively high selectivity ratios (SF) for monovalent/divalent ion pairs (Stage 2), such as $SFLi^+/Mg^{2+}$ = 5.14 and $SFNa^+/Mg^{2+}$ = 5.69. Upon PDA-only modification (M1), these values increased modestly (e.g., $SFNa^+/Mg^{2+}$ = 7.58), indicating improved differentiation between mono- and divalent ions. M2, with balanced PDA and PEI content (1:1), exhibited the highest selectivity across all tested ion pairs, reaching a peak $SFNa^+/Mg^{2+}$ of 10.00 and $SFLi^+/Ca^{2+}$ of 7.44. The results demonstrate that the presence of PEI in membrane M2 significantly enhances SF. This improvement is attributed to the positively charged nature of PEI, which modulates the surface charge balance of the membrane, promoting electrostatic interactions that favor selective ion separation. A similar strategy was employed by Li et al. to improve the separation performance of single salt solutions in their study [62,63].

However, at higher PEI content (M3), a slight decline in selectivity was observed for some ion pairs (e.g., $SFLi^+/Mg^{2+}$ = 4.96, $SFNa^+/Mg^{2+}$ = 4.11), despite a higher rejection of both mono- and divalent ions. The observed reduction is likely due to excessive PEI loading, which can result in over-compaction of the surface layer or partial pore blockage. Similar findings were reported by He et al., where an excess of PEI monomers led to the formation of oligomers that penetrated or accumulated within the selective layer pores, thereby reducing membrane permeability [64].

Overall, the modification with PDA–PEI significantly improved both the salt rejection and ion selectivity of the commercial NF membrane, with the best performance observed at a PDA:PEI ratio of 1:1 (M2), suggesting this composition offers an optimal trade-off between charge density, hydrophilicity, and permeability.

The ion selectivity behavior of M0 was systematically evaluated under the influence of inorganic foulants gypsum, silica, and their combination within multi–ion solution, and compared to a control solution without foulants (Stage 3). As shown in Fig. 6C, the presence and nature of foulants had a significant impact on the membrane's monovalent/divalent ion selectivity. Specifically, the lithium over magnesium selectivity ($SFLi^{+}/Mg^{2+}$) decreased progressively with the introduction of foulants, from 5.76 in the absence of foulants to 4.51 with gypsum, 4.88 with silica, and further to 4.48 with the gypsum–silica combination. In contrast, an anomalous trend was observed for $SFLi^{+}/Ca^{2+}$, which increased from 3.56 in the control solution to 7.80, 5.82, and 6.12 in the presence of gypsum, silica, and their combination, respectively.

The general decline in selectivity for other monovalent/divalent ion pairs such as Na^{+}/Mg^{2+}, Na^{+}/Ca^{2+}, K^{+}/Mg^{2+}, and K^{+}/Ca^{2+} across all fouling conditions further indicates that the dominant foulant layers broadly influence monovalent ion transport, not limited to lithium. Detailed selectivity data are provided in Table S1.

These variations in selectivity can be explained by the physicochemical impacts of the foulants on membrane surface properties. Gypsum deposition alters the surface charge distribution, leading to compression of the electrical double layer [65], and its crystallization may block pores, thereby disturbing the steric hindrance mechanisms crucial for selective separation. Furthermore, silica tends to form a gel–like fouling layer characterized by high hydraulic resistance, which weakens charge-based selectivity by enhancing concentration polarization at the membrane surface and facilitating undesired ion diffusion. Similar fouling-induced performance declines have been documented by Lee et al. in their study on salt–silica interactions in nanofiltration and reverse osmosis membranes [66].

In addition to ion selectivity and rejection performance, the long-term operational stability of the membrane was evaluated through cyclic permeability testing, focusing on the pristine membrane (M0) and modified membranes (M1–M3). The objective was to investigate the fouling resistance and permeability recovery following repeated exposure to fouling agents, as outlined in Section 2.4.

For M0, fouling was assessed in the presence of model foulants, including gypsum, silica, and a combined gypsum–silica mixture. As shown in Fig. S6A, the M0 membrane exhibited a consistent decline in PWP across all cycles, indicating progressive fouling and poor reversibility. During the first cycle, PWP remained stable between 25.04 and 24.83 $L{\cdot}m^{-2}{\cdot}h^{-1}{\cdot}bar^{-1}$ for the first 60 min under clean water conditions. However, when tested with a salts-silica solution, permeability decreased significantly from 8.94 to 7.55 $L{\cdot}m^{-2}{\cdot}h^{-1}{\cdot}bar^{-1}$, highlighting the onset of fouling, likely due to silica gel layer formation on the membrane surface.

A standard flushing–backwash procedure was then applied for 10 min, followed by re-measurement of PWP. Despite partial recovery to 18.63–17.31 $L{\cdot}m^{-2}{\cdot}h^{-1}{\cdot}bar^{-1}$, successive testing cycles (cycles 2 to 4) showed a gradual decline in final PWP values to 6.99, 6.55, and 6.33 $L{\cdot}m^{-2}{\cdot}h^{-1}{\cdot}bar^{-1}$, respectively. Similar trends were observed for gypsum and gypsum–silica systems (Fig. S6B–C), confirming the strong interaction between the foulants and the pristine polyamide surface. The limited recovery of M0 can be attributed to irreversible fouling mechanisms such as pore blockage, foulant adsorption, and cake layer compaction. The average permeability degradation trend for M0 is summarized in Fig. 7A–B.

To address this limitation, surface modification using PDA-PEI was employed, with M2 (PDA:PEI = 1:1) selected for antifouling performance testing using both SGB and RGB. As shown in Fig. 7C–D, permeability in M2 also exhibited a decreasing trend over four cycles, which is expected due to the complex foulant composition including silica and gypsum. However, a notable improvement in permeability recovery was observed after flushing–backwash treatments. Although full recovery to initial PWP values was not achieved, the modified membrane demonstrated a significantly better resistance to fouling–induced decline compared to M0. The results further confirm that the hydrophilic functional groups (–OH and $–NH_2$) introduced through

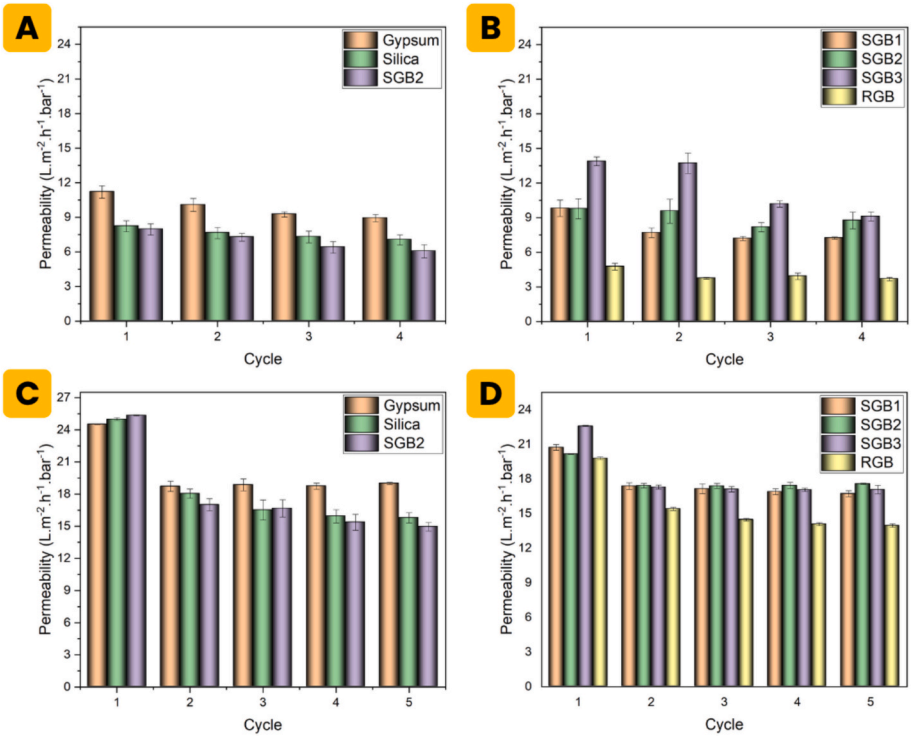

Fig. 7. Average permeability performance of membranes: (A–B) pristine membrane (M0) in sample solution, and (C–D) modified membrane (M2) in pure water.

PDA–PEI co–deposition play a critical role in enhancing the membrane's antifouling properties [53,67,68]. These functional groups facilitate the formation of a hydration layer on the membrane surface, which serves as a physical barrier that hinders foulant adhesion. Moreover, the increased surface hydrophilicity is accompanied by the development of a strong negative surface charge, which contributes to antifouling performance by inducing electrostatic repulsion against negatively charged foulants.

To complement the analysis, the proposed mechanism of membrane scaling resulting from gypsum crystallization and silica deposition is illustrated in Fig. 8. As water permeates through the membrane, a concentration polarization layer develops near the surface, leading to local ion accumulation and restricted ionic mobility. Within this confined region, ionic interactions promote the initial nucleation of gypsum crystals under unstable conditions. These imperfect crystals, driven by hydraulic flow, adhere to the membrane surface and collide with one another, gradually forming dense crystalline deposits. In parallel, silica scaling is initiated through polymerization of silicic acid species in the aqueous phase near the membrane. While some polymerization occurs in the bulk, additional growth proceeds directly on the membrane surface, where continuous bonding leads to the formation of a scaffold–like polysilicic acid layer. LRO membrane characterized by a negatively charged and hydrophilic surface (as described in previous sections), demonstrates effective resistance against gypsum crystal adhesion. However, this modification remains insufficient to fully prevent the formation and anchoring of the more persistent silica polymer network.

Despite the improved antifouling performance of the M2 membrane, residual impurities remained on its surface after cleaning, as confirmed by SEM–EDX analysis (Fig. S8). The analysis revealed trace but detectable amounts of Ca and Si, which were identified as the primary foulants. These elements exhibited a relatively uniform distribution across the membrane surface, suggesting potential interactions or co–deposition during filtration. In contrast, M0 analyzed via SEM (Fig. 9A), displayed a significantly higher accumulation of foulants under identical testing conditions compared to M2 (Fig. 9E), highlighting the benefit of surface modification.

Furthermore, in the specific cases of SGB2 and RGB samples, AFM characterization provided deeper insight into surface morphology changes due to fouling (Fig. 9D&E). The RGB–treated membrane exhibited a more homogeneous foulant coverage compared to SGB2, consistent with the SEM–EDX findings. Sa increased markedly from the initial value of approximately 6 nm to 18.99 ± 3.38 nm after exposure to SGB2, and further to 28.49 ± 2.16 nm following treatment with RGB solution.

The antifouling performance of the membranes was assessed by measuring FRR over five operational cycles, including four cycles of fouling followed by one cleaning cycle through backwashing, as illustrated in Fig. 10. M0 demonstrated an FRR of 77.52 % when tested with the gypsum–multi-ion solution, indicating relatively reversible fouling.

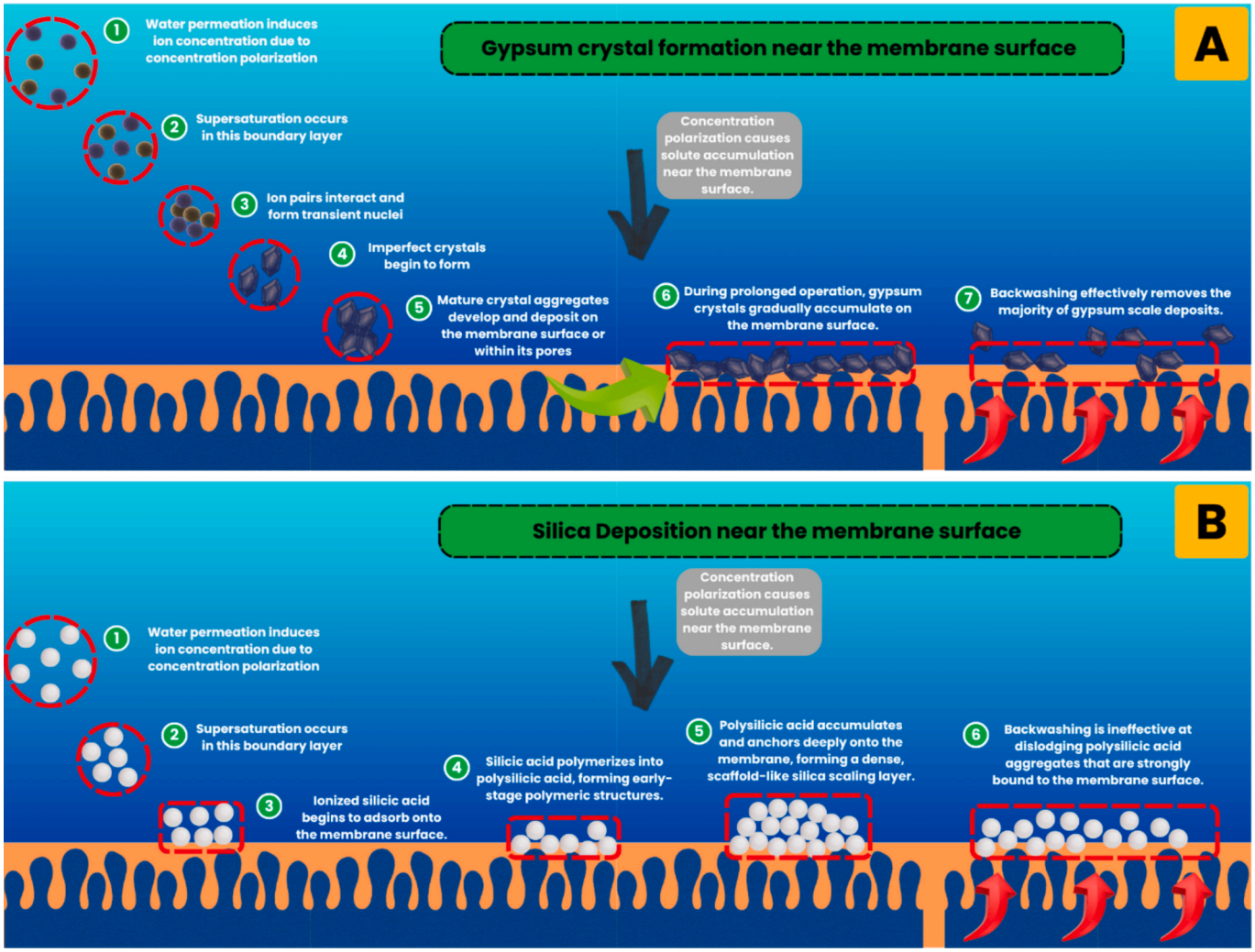

Fig. 8. Surface characteristics of membrane scaling: (a) gypsum crystal formation and (b) silica deposition.

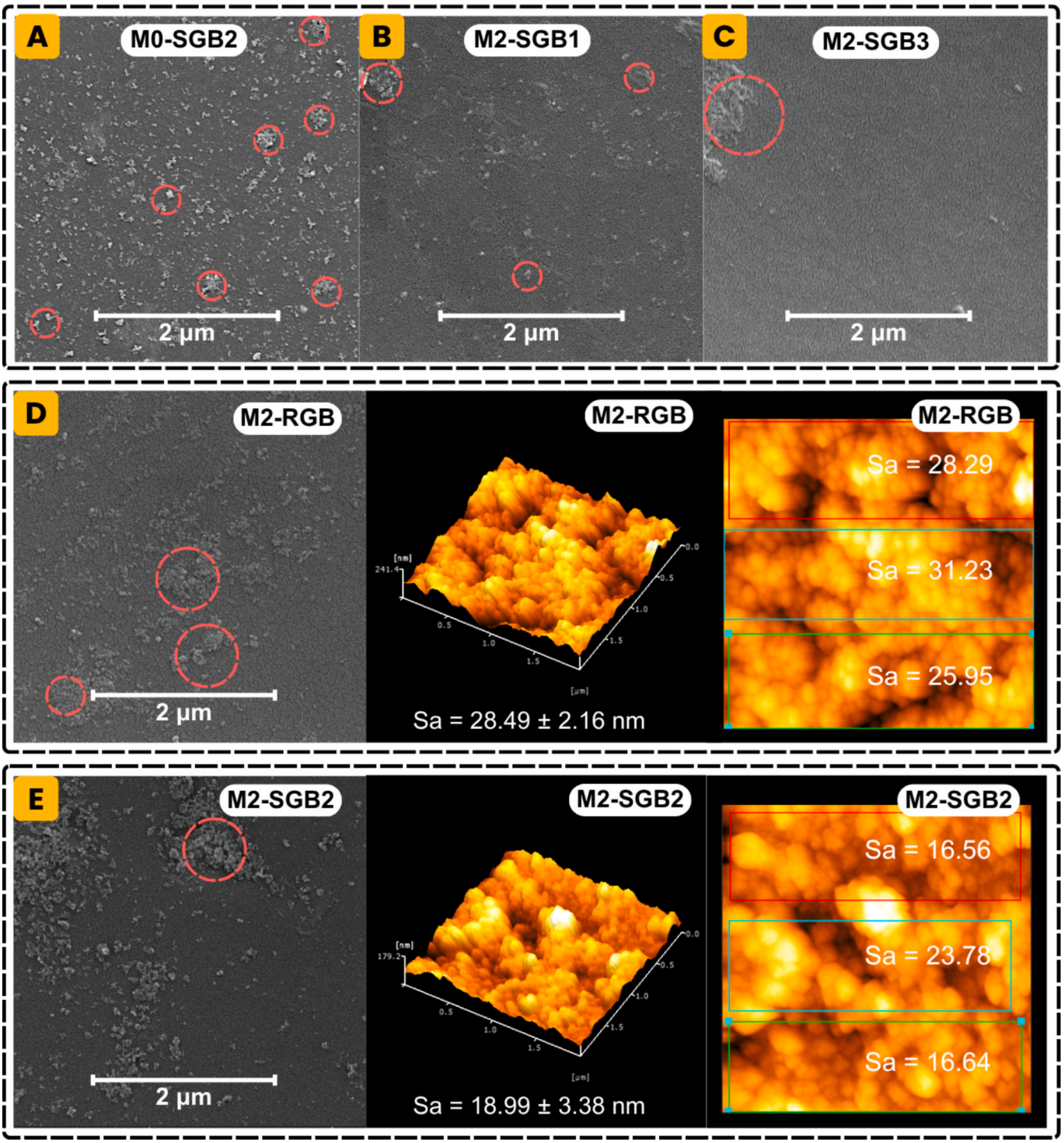

Fig. 9. Surface characterization of membranes after four filtration cycles: SEM morphology of M0 and M2 in SGB and RGB, and AFM topography of M2 in SGB and RGB.

However, a reduced FRR of 63.12 % was observed for the silica–multi-ion solution, suggesting more persistent fouling. The most severe fouling was observed with SGB2, which led to a further decrease in FRR to 58.99 %.

In contrast, the PDA–PEI modified membrane (M2) exhibited significantly improved antifouling behavior, with an FRR of 87.18 % in SGB2. Enhanced flux recovery was also observed under other conditions, with FRRs of 80.65 % in SGB1, 75.56 % in SGB3, and 95.33 % in real geothermal brine (RGB), confirming the superior fouling resistance imparted by PDA–PEI surface modification.

Beyond antifouling performance, the effectiveness of membrane separation was further evaluated through the selectivity–permeability trade-off, particularly $SFLi^{+}/Mg^{2+}$. As detailed in Table S2, the modified commercial NF membrane achieved a maximum $SFLi^{+}/Mg^{2+}$ of 7.83 at a permeability of 22.5 $L{\cdot}m^{-2}{\cdot}h^{-1}{\cdot}bar^{-1}$ (See Fig. 11). These findings underscore the dual enhancement in both antifouling performance and selective separation, which are critical for guiding future membrane design and optimization in complex feed environments such as

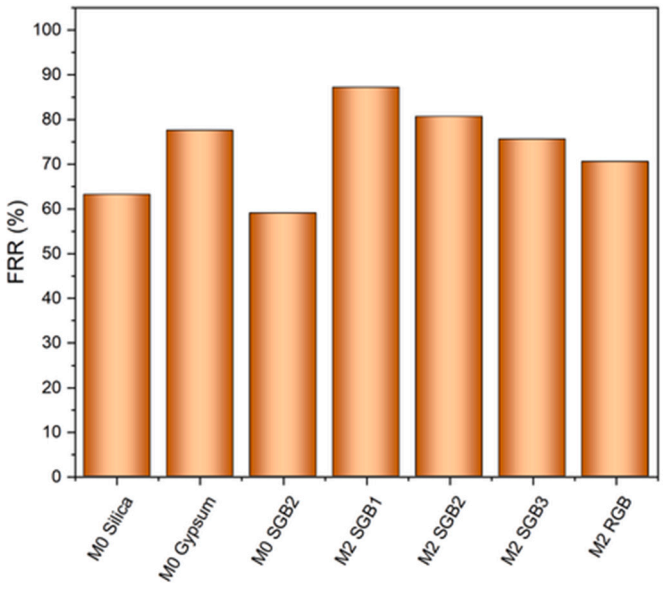

Fig. 10. Flux recovery ratio (FRR) of pristine (M0) and modified membranes (M1–M3) under various test solution conditions, illustrating antifouling performance.

geothermal brines.

3.3. Future research

Further development of membrane technology for lithium separation from geothermal brine will focus on investigating the influence of polyethyleneimine (PEI) molecular weight and co-deposition time on the membrane's physical and chemical properties. These variables are expected to significantly affect critical characteristics such as film thickness, hydrodynamic diameter, surface roughness, contact angle, and other parameters relevant to ion selectivity and transport. In addition, long-term membrane performance testing will be conducted to assess stability and durability under extended operational conditions. Complementary economic and environmental assessments will also be carried out to evaluate the feasibility of large-scale implementation. It is recognized that achieving high lithium/magnesium selectivity is necessary but not sufficient broader considerations including process sustainability, cost-effectiveness, and operational longevity are equally vital for the successful translation of this technology to industrial applications.

4. Conclusions

This study demonstrated the successful fabrication of loose reverse osmosis (LRO) membranes via PDA–PEI co–deposition on commercial NF membranes for lithium extraction from geothermal brine. The modification enhanced membrane hydrophilicity, reduced pore size, and improved antifouling performance, key to mitigating challenges from foulants like gypsum and silica. Among tested variants, the M2 membrane (PDA:PEI = 1:1) exhibited the most favorable surface characteristics, including uniform coating and functional group integration. This formulation effectively suppressed PDA aggregation and ensured a well-distributed copolymer layer.

Performance tests showed M2 achieved a pure water permeability of 22.5 $L{\cdot}m^{-2}{\cdot}h^{-1}{\cdot}bar^{-1}$ and superior ion rejection, with Li^{+}/Mg^{2+} selectivity reaching 7.83, indicating enhanced monovalent/divalent ion separation. Multicycle fouling tests using both simulated and real geothermal brine confirmed improved fouling resistance and high flux recovery ratios. Surface analyses (SEM–EDX, AFM) verified lower foulant deposition and preserved membrane structure after prolonged operation. The PDA–PEI co-deposition process is simple, environmentally friendly, and compatible with commercial substrates, making it a promising strategy for scalable and sustainable lithium recovery applications.

CRediT authorship contribution statement

Pra Cipta Buana Wahyu Mustika: Writing – original draft, Visualization, Validation, Methodology, Investigation. **Richard Sudarmanto:** Investigation. **Hansdersen Hermes Irawan:** Investigation. **Ariel Halim Qiu:** Investigation. **Putu Doddy Sutrisna:** Writing – review & editing, Supervision, Conceptualization. **Sutijan Sutijan:** Writing – review & editing, Supervision. **Widi Astuti:** Writing – review & editing, Supervision, Resources, Formal analysis. **Siti Nurul Aisyiyah Jenie:** Resources, Formal analysis. **Khoiruddin Khoiruddin:** Writing – review & editing, Resources, Formal analysis. **Himawan Tri Bayu Murti Petrus:** Writing – review & editing, Supervision, Resources, Project administration, Funding acquisition.

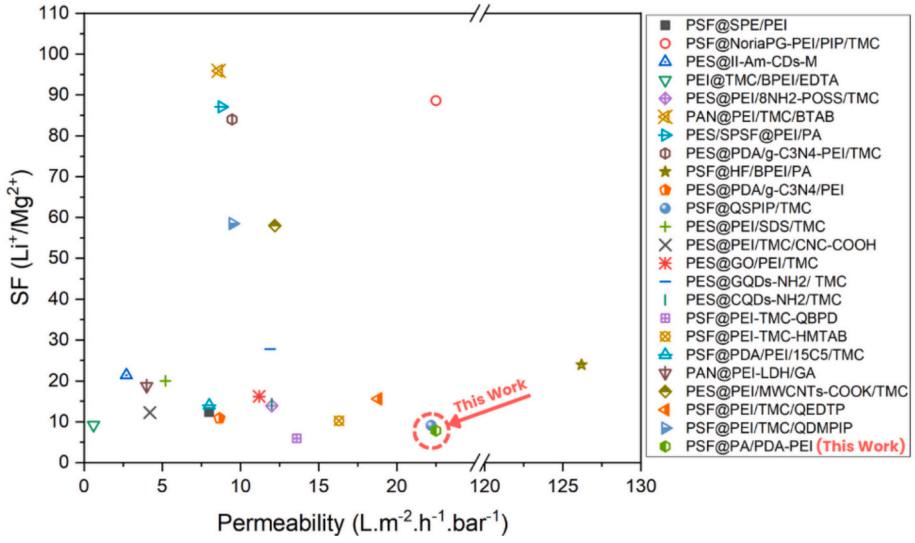

Fig. 11. Selectivity–permeability trade-off comparison between the present study and previously reported modified membranes. Detailed numerical data are provided in Table S2.

Declaration of Generative AI and AI-assisted technologies in the writing process

In the preparation of this work, the author(s) utilized ChatGPT 4.0 to enhance readability and language clarity. Following its use, the author (s) thoroughly reviewed and revised the content as necessary, assuming full responsibility for the final version of the publication.

Declaration of competing interest

The authors declare that they have no known competing financial interests or personal relationships that could have appeared to influence the work reported in this paper.

Acknowledgments

This research was entirely supported by Universitas Gadjah Mada (UGM). The authors also express their gratitude to Universitas Surabaya (UBAYA) and Institut Teknologi Bandung (ITB) for their valuable analytical assistance and access to laboratory facilities, which played a crucial role in the successful completion of this study.

Appendix A. Supplementary data

Supplementary data to this article can be found online at https://doi.org/10.1016/j.jwpe.2025.108458.

Data availability

Data will be made available on request.

References

[1] S. Priyadarsini, A.P. Das, Lithium bioleaching: a review on microbial-assisted sustainable technology for lithium bio-circularity, J. Water Process Eng. 69 (2025) 106744, https://doi.org/10.1016/j.jwpe.2024.106744.
[2] R. Reich, K. Slunitschek, R.M. Danisi, E. Eiche, J. Kolb, Lithium extraction techniques and the application potential of different sorbents for lithium recovery from brines, Miner. Process. Extr. Metall. Rev. 44 (2023) 261–280, https://doi.org/10.1080/08827508.2022.2047041.
[3] J. Cabello, Lithium brine production, reserves, resources and exploration in Chile: an updated review, Ore Geol. Rev. 128 (2021) 103883, https://doi.org/10.1016/j.oregeorev.2020.103883.
[4] B. Zhang, F. yu Qi, X. zheng Gao, X. lei Li, Y. tao Shang, Z. yu Kong, L. qiong Jia, J. Meng, H. Guo, F. kang Fang, Y. bin Liu, X. Jiang, H. Chai, Z. Liu, X. tao Ye, G. dong Wang, Geological characteristics, metallogenic regularity, and research progress of lithium deposits in China, China Geol. 5 (2022) 734–767, https://doi.org/10.31035/cg2022054.
[5] B. Sanjuan, B. Gourcerol, R. Millot, D. Rettenmaier, E. Jeandel, A. Rombaut, Lithium-rich geothermal brines in Europe: an up-date about geochemical characteristics and implications for potential Li resources, Geothermics 101 (2022) 102385, https://doi.org/10.1016/j.geothermics.2022.102385.
[6] M. Marza, G. Ferguson, J. Thorson, I. Barton, J.-H. Kim, L. Ma, J. McIntosh, Geological controls on lithium production from basinal brines across North America, J. Geochem. Explor. 257 (2024) 107383, https://doi.org/10.1016/j.gexplo.2023.107383.
[7] E.S. Rentier, C. Hoorn, A.C. Seijmonsbergen, Lithium brine mining affects geodiversity and Sustainable Development Goals, Renew. Sust. Energ. Rev. 202 (2024) 114642, https://doi.org/10.1016/j.rser.2024.114642.
[8] D.P.A. Sudarmaja, C.E. Suryanaga, V.S.H. Sujoto, S.N.A. Jenie, W. Astuti, F. Anggara, A. Prasetya, Sutijan, H.T.B.M. Petrus, Enhancing lithium concentration performance from synthetic geothermal brine through electro-nanofiltration method, Chem. Eng. J. 516 (2025) 164134, https://doi.org/10.1016/j.cej.2025.164134.
[9] Y. Sun, Q. Wang, Y. Wang, R. Yun, X. Xiang, Recent advances in magnesium/lithium separation and lithium extraction technologies from salt lake brine, Sep. Purif. Technol. 256 (2021) 117807, https://doi.org/10.1016/j.seppur.2020.117807.
[10] M.R. Mojid, K.J. Lee, J. You, A review on advances in direct lithium extraction from continental brines: ion-sieve adsorption and electrochemical methods for varied Mg/Li ratios, Sustain. Mater. Technol. 40 (2024) e00923, https://doi.org/10.1016/j.susmat.2024.e00923.
[11] A. Khalil, S. Mohammed, R. Hashaikeh, N. Hilal, Lithium recovery from brine: recent developments and challenges, Desalination 528 (2022) 115611, https://doi.org/10.1016/j.desal.2022.115611.
[12] R. Tscherning, B. Chapman, Navigating the emerging lithium rush: lithium extraction from brines for clean-tech battery storage technologies, J. Energy Nat. Resour. Law 39 (2021) 13–42, https://doi.org/10.1080/02646811.2020.1841399.
[13] S. Lanjewar, A. Mukherjee, P. Khandewal, A.K. Ghosh, A. Mullick, S. Moulik, A. Roy, Thermodynamics of synthesis and separation performance of Interfacially polymerized "loose" reverse osmosis membrane: benchmarking for greywater treatment, Chem. Eng. J. 417 (2021) 127929, https://doi.org/10.1016/j.cej.2020.127929.
[14] Q.-M. Nguyen, S. Jeong, S. Lee, Characteristics of membrane foulants at different degrees of SWRO brine concentration by membrane distillation, Desalination 409 (2017) 7–20, https://doi.org/10.1016/j.desal.2017.01.007.
[15] Q.-M. Nguyen, S. Lee, Fouling analysis and control in a DCMD process for SWRO brine, Desalination 367 (2015) 21–27, https://doi.org/10.1016/j.desal.2015.03.039.
[16] Y. Li, M. Wang, X. Xiang, Y.J. Zhao, Z.J. Peng, Separation performance and fouling analyses of nanofiltration membrane for lithium extraction from salt lake brine, J. Water Process Eng. 54 (2023) 104009, https://doi.org/10.1016/j.jwpe.2023.104009.
[17] P.C.B.W. Mustika, P.D. Sutrisna, S. Sutijan, H.T.B.M. Petrus, S. Sumardi, W. Astuti, Understanding membrane fouling in pressure-driven and thermal-driven processes for brines applications: challenges, mechanisms, characterization, mitigation strategies, and future perspectives, J. Water Process Eng. 72 (2025) 107631, https://doi.org/10.1016/j.jwpe.2025.107631.
[18] S.J. Einarsson, L. Guan, L.N. Sim, T.H. Chong, B. Wu, Fouling behaviours and mitigation in pressure-retarded osmosis processes with geothermal water/brine-based draw solutions, J. Water Process Eng. 51 (2023) 103485, https://doi.org/10.1016/j.jwpe.2023.103485.
[19] S. Mestri, T.P.P. Le, M.S. Jouini, F. AlMarzooqi, S.W. Hasan, E. Alhseinat, Surface modification of nanofiltration membrane for enhancing salt rejection and scaling remediation in brackish groundwater desalination application, Desalination 598 (2025) 118417, https://doi.org/10.1016/j.desal.2024.118417.
[20] N. Shahkaramipour, T. Tran, S. Ramanan, H. Lin, Membranes with surface-enhanced antifouling properties for water purification, Membranes (Basel) 7 (2017) 13, https://doi.org/10.3390/membranes7010013.
[21] J. Wang, X. Wang, Z. Liu, P. Sun, Y. Hou, N. Wang, L. Wang, Mitigation mechanisms of silica scaling on different organic-fouled nanofiltration membrane surface, Colloids Surf. A Physicochem. Eng. Asp. 686 (2024) 133298, https://doi.org/10.1016/j.colsurfa.2024.133298.
[22] R.R. Choudhury, J.M. Gohil, S. Mohanty, S.K. Nayak, Antifouling, fouling release and antimicrobial materials for surface modification of reverse osmosis and nanofiltration membranes, J. Mater. Chem. A 6 (2018) 313–333, https://doi.org/10.1039/C7TA08627J.
[23] S.M.H. Gowayed, A.H. Abdel-Salam, E. Nassef, A. Morsy, Innovative hybrid membrane: pioneering metal oxide framework for improved elimination of heavy metals from industrial wastewater, Polym. Eng. Sci. 65 (2025) 2093–2105, https://doi.org/10.1002/pen.27139.
[24] E.A. Fadl, O. Elsahy, S. Kandil, A. Morsy, Enhancing the performance and antifouling properties of reverse osmosis membranes by graphene quantum dots for water desalination, Appl Water Sci 15 (2025) 84, https://doi.org/10.1007/s13201-025-02410-8.
[25] Z. Yan, Y. Zhang, H. Yang, G. Fan, A. Ding, H. Liang, G. Li, N. Ren, B. Van der Bruggen, Mussel-inspired polydopamine modification of polymeric membranes for the application of water and wastewater treatment: a review, Chem. Eng. Res. Des. 157 (2020) 195–214, https://doi.org/10.1016/j.cherd.2020.03.011.
[26] S. Chen, P. Liu, Z. Li, N. Tang, T. Li, Y. Yu, F. Li, Y. Bi, Preparation and performance of composite nanofiltration membrane modified by mussel coating, J. Polym. Environ. 31 (2023) 5089–5098, https://doi.org/10.1007/s10924-023-02928-5.
[27] H. Karkhanechi, R. Takagi, H. Matsuyama, Biofouling resistance of reverse osmosis membrane modified with polydopamine, Desalination 336 (2014) 87–96, https://doi.org/10.1016/j.desal.2013.12.033.
[28] Q. Huang, J. Chen, M. Liu, H. Huang, X. Zhang, Y. Wei, Polydopamine-based functional materials and their applications in energy, environmental, and catalytic fields: state-of-the-art review, Chem. Eng. J. 387 (2020) 124019, https://doi.org/10.1016/j.cej.2020.124019.
[29] L. Ma, Q. Bi, Y. Tang, C. Zhang, F. Qi, H. Zhang, Y. Gao, S. Xu, Fabrication of high-performance nanofiltration membrane using polydopamine and carbon nitride as the interlayer, Separations 9 (2022) 180, https://doi.org/10.3390/separations9070180.
[30] X. Yang, Y. Du, X. Zhang, A. He, Z.-K. Xu, Nanofiltration membrane with a mussel-inspired interlayer for improved permeation performance, Langmuir 33 (2017) 2318–2324, https://doi.org/10.1021/acs.langmuir.6b04465.
[31] Z. Yang, F. Wang, H. Guo, L.E. Peng, X. Ma, X. Song, Z. Wang, C.Y. Tang, Mechanistic insights into the role of polydopamine interlayer toward improved separation performance of polyamide nanofiltration membranes, Environ. Sci. Technol. 54 (2020) 11611–11621, https://doi.org/10.1021/acs.est.0c03589.
[32] D.L. Zhao, Q. Zhao, H. Lin, S.B. Chen, T.-S. Chung, Pressure-assisted polydopamine modification of thin-film composite reverse osmosis membranes for enhanced desalination and antifouling performance, Desalination 530 (2022) 115671, https://doi.org/10.1016/j.desal.2022.115671.
[33] Y. Qi, L. Zhu, C. Gao, J. Shen, A novel nanofiltration membrane with simultaneously enhanced antifouling and antibacterial properties, RSC Adv. 9 (2019) 6107–6117, https://doi.org/10.1039/C8RA09875A.
[34] J. Wang, J. Zhu, M.T. Tsehaye, J. Li, G. Dong, S. Yuan, X. Li, Y. Zhang, J. Liu, B. Van der Bruggen, High flux electroneutral loose nanofiltration membranes based on rapid deposition of polydopamine/polyethyleneimine, J. Mater. Chem. A Mater. 5 (2017) 14847–14857, https://doi.org/10.1039/C7TA02661G.

[35] J. Wang, H. Guo, X. Shi, Z. Yao, W. Qing, F. Liu, C.Y. Tang, Fast polydopamine coating on reverse osmosis membrane: process investigation and membrane performance study, J. Colloid Interface Sci. 535 (2019) 239–244, https://doi.org/10.1016/j.jcis.2018.10.016.
[36] L. Gao, H. Wang, Y. Zhang, M. Wang, Nanofiltration membrane characterization and application: extracting lithium in Lepidolite leaching solution, Membranes 10 (2020) 178, https://doi.org/10.3390/membranes10080178.
[37] E.Q. Lim, M.Q. Seah, W.J. Lau, H. Hasbullah, P.S. Goh, A.F. Ismail, D. Emadzadeh, Evaluation of surface properties and separation performance of NF and RO membranes for phthalates removal, Membranes (Basel) 13 (2023) 413, https://doi.org/10.3390/membranes13040413.
[38] F.A. Setiawan, E. Rahayuningsih, H.T.B.M. Petrus, M.I. Nurpratama, I. Perdana, Kinetics of silica precipitation in geothermal brine with seeds addition: minimizing silica scaling in a cold re-injection system, Geotherm. Energy 7 (2019), https://doi.org/10.1186/s40517-019-0138-3.
[39] W. Liu, X. Huang, K. Peng, Y. Xiong, J. Zhang, L. Lu, J. Liu, S. Li, PDA-PEI copolymerized highly hydrophobic sponge for oil-in-water emulsion separation via oil adsorption and water filtration, Surf. Coat. Technol. 406 (2021) 126743, https://doi.org/10.1016/j.surfcoat.2020.126743.
[40] Y. Lv, H.-C. Yang, H.-Q. Liang, L.-S. Wan, Z.-K. Xu, Nanofiltration membranes via co-deposition of polydopamine/polyethylenimine followed by cross-linking, J. Membr. Sci. 476 (2015) 50–58, https://doi.org/10.1016/j.memsci.2014.11.024.
[41] H.-C. Yang, K.-J. Liao, H. Huang, Q.-Y. Wu, L.-S. Wan, Z.-K. Xu, Mussel-inspired modification of a polymer membrane for ultra-high water permeability and oil-in-water emulsion separation, J. Mater. Chem. A 2 (2014) 10225–10230, https://doi.org/10.1039/C4TA00143E.
[42] P.D. Sutrisna, P.C.B.W. Mustika, R.P. Hadi, Caren, Y.E. Gani, Improved oily wastewater rejection and flux of hydrophobic PVDF membrane after polydopamine-polyethyleneimine co-deposition and modification, S. Afr. J. Chem. Eng. 44 (2023) 42–50, https://doi.org/10.1016/j.sajce.2023.01.006.
[43] Y. Lv, Y. Du, Z.-X. Chen, W.-Z. Qiu, Z.-K. Xu, Nanocomposite membranes of polydopamine/electropositive nanoparticles/polyethyleneimine for nanofiltration, J. Membr. Sci. 545 (2018) 99–106, https://doi.org/10.1016/j.memsci.2017.09.066.
[44] Z. Wang, W. Zhang, S. Wen, L. Wang, S. Wang, Y. Wang, J. Lu, J. Ma, W. Cheng, Rapid co-deposition of dopamine and polyethyleneimine triggered by CuSO4/H2O2 oxidation to fabricate nanofiltration membranes with high selectivity and antifouling ability, Sep. Purif. Technol. 305 (2023) 122409, https://doi.org/10.1016/j.seppur.2022.122409.
[45] H. Li, L. Peng, Y. Luo, P. Yu, Enhancement in membrane performances of a commercial polyamide reverse osmosis membrane via surface coating of polydopamine followed by the grafting of polyethylenimine, RSC Adv. 5 (2015) 98566–98575, https://doi.org/10.1039/C5RA20891B.
[46] M.A. Ashraf, J. Wang, B. Wu, P. Cui, B. Xu, X. Li, Enhancement in Li + /Mg 2+ separation from salt lake brine with PDA–PEI composite nanofiltration membrane, J. Appl. Polym. Sci. 137 (2020), https://doi.org/10.1002/app.49549.
[47] A. Eltahan, N. Ismail, M. Khalil, S. Ebrahim, M. Soliman, E. Nassef, A. Morsy, Advanced fabrication and characterization of thin-film composite polyamide membranes for superior performance in reverse osmosis desalination, Sci. Rep. 15 (2025) 15131, https://doi.org/10.1038/s41598-025-97871-x.
[48] Z. Mi, Z. Liu, S. Jin, D. Zhang, D. Wang, Positively charged nanofiltration membrane prepared by polydopamine deposition followed by crosslinking for high efficiency cation separation, Polym. Test. 93 (2021) 107000, https://doi.org/10.1016/j.polymertesting.2020.107000.
[49] J. Zhu, M.T. Tsehaye, J. Wang, A. Uliana, M. Tian, S. Yuan, J. Li, Y. Zhang, A. Volodin, B. Van der Bruggen, A rapid deposition of polydopamine coatings induced by iron (III) chloride/hydrogen peroxide for loose nanofiltration, J. Colloid Interface Sci. 523 (2018) 86–97, https://doi.org/10.1016/j.jcis.2018.03.072.
[50] J. Farahbakhsh, V. Vatanpour, M. Khoshnam, M. Zargar, Recent advancements in the application of new monomers and membrane modification techniques for the fabrication of thin film composite membranes: a review, React. Funct. Polym. 166 (2021) 105015, https://doi.org/10.1016/j.reactfunctpolym.2021.105015.
[51] D.D. Al-Araji, F.H. Al-Ani, Q.F. Alsalhy, Polyethyleneimine (PEI) grafted silica nanoparticles for polyethersulfone membranes modification and their outlooks for wastewater treatment - a review, Int. J. Environ. Anal. Chem. 103 (2023) 4752–4776, https://doi.org/10.1080/03067319.2021.1931163.
[52] D. Yu, M. Li, H. Zhou, X. Liang, Q. Shou, H. Liu, Polyamide composite nanofiltration membrane via a combination of polydopamine grafting and reverse interfacial polymerization for high Mg2+/Li+ separation capacity, Sep. Purif. Technol. 355 (2025) 129746, https://doi.org/10.1016/j.seppur.2024.129746.
[53] H. Jia, J. Ren, Y. Kong, Z. Ji, S. Guo, J. Li, Recent advances in dopamine-based membrane surface modification and its membrane distillation applications, Membranes (Basel) 14 (2024) 81, https://doi.org/10.3390/membranes14040081.
[54] P. Li, Y. Zhou, C. Hai, Y. Tang, Y. Cheng, Y. Sun, S. Dong, L. Ma, X. He, Q. Xu, High-flux polyamide nanofiltration membranes tuning by polydopamine-modified boron nitride nanosheets: accelerating Mg2+/Li+ separation, Sep. Purif. Technol. 356 (2025) 129917, https://doi.org/10.1016/j.seppur.2024.129917.
[55] B. Tansel, Significance of thermodynamic and physical characteristics on permeation of ions during membrane separation: hydrated radius, hydration free energy and viscous effects, Sep. Purif. Technol. 86 (2012) 119–126, https://doi.org/10.1016/j.seppur.2011.10.033.
[56] D. Lu, Z. Yao, L. Jiao, M. Waheed, Z. Sun, L. Zhang, Separation mechanism, selectivity enhancement strategies and advanced materials for mono-/multivalent ion-selective nanofiltration membrane, Adv. Membr. 2 (2022), https://doi.org/10.1016/j.advmem.2022.100032.
[57] A. Al-Saadi, H. Mousa, G.R. Vakili-Nezhaad, A.M. Gujarathi, Experimental investigation of the effect of ion concentration and its valence on reflection coefficient and solute permeability of NF membranes, Desalin. Water Treat. 212 (2021) 276–285, https://doi.org/10.5004/dwt.2021.26642.
[58] O.P. Crossley, R.B. Thorpe, D. Peus, J. Lee, The effect of salinity on the pressure susceptibility of the NF270 membrane, Desalination 564 (2023) 116804, https://doi.org/10.1016/j.desal.2023.116804.
[59] X. Shi, Q. Zhang, Z. Wang, Q. Bi, Y. Lin, Acetone-modulated reverse interfacial polymerization was employed to prepare PEI/PDA positively charged composite nanofiltration membranes for Mg2+/Li+ separation, J. Membr. Sci. 720 (2025) 123780, https://doi.org/10.1016/j.memsci.2025.123780.
[60] W. Li, J. Liu, W. Wang, S. Chen, F. Jia, X. Li, Y. Zhao, W. Zhang, D. Song, J. Ma, Tailoring the performance of a composite PEI nanofiltration membrane via incorporating activated PDA for efficient dye sieving and salt separation, Membranes (Basel) 15 (2025) 75, https://doi.org/10.3390/membranes15030075.
[61] Y. Zhang, S. Huang, B. Mei, X. Tian, L. Jia, W. Zhu, Mussel inspired synthesis of polydopamine/polyethyleneimine-grafted fly ash composite adsorbent for the effective separation of U(VI), Sci. Total Environ. 876 (2023) 162841, https://doi.org/10.1016/j.scitotenv.2023.162841.
[62] C. Li, Q. Yang, D. Chen, H. Zhu, J. Chen, R. Liu, Q. Dang, X. Wang, Polyethyleneimine-assisted co-deposition of polydopamine coating with enhanced stability and efficient secondary modification, RSC Adv. 12 (2022) 34837–34849, https://doi.org/10.1039/D2RA05130C.
[63] S. Li, C. Zheng, L. Tu, D. Cai, Y. Huang, C. Gao, Y. Lu, L. Xue, Construction of PDA-PEI/ZIF-L@PE tight ultra-filtration (TUF) membranes on porous polyethylene (PE) substrates for efficient dye/salt separation, J. Hazard. Mater. 468 (2024) 133727, https://doi.org/10.1016/j.jhazmat.2024.133727.
[64] J. He, Y. Wang, F. Ni, F. Shen, S. Deng, Y. Zhang, L. Long, L. Luo, Y. Liu, Ultra-highly permeable loose nanofiltration membrane containing PG/PEI/Fe3+ ternary coating for efficient dye/salt separation, Sep. Purif. Technol. 292 (2022) 121020, https://doi.org/10.1016/j.seppur.2022.121020.
[65] C.Y. Tang, T.H. Chong, A.G. Fane, Colloidal interactions and fouling of NF and RO membranes: a review, Adv. Colloid Interf. Sci. 164 (2011) 126–143, https://doi.org/10.1016/j.cis.2010.10.007.
[66] S. Lee, J. Cho, M. Elimelech, Influence of colloidal fouling and feed water recovery on salt rejection of RO and NF membranes, Desalination 160 (2004) 1–12, https://doi.org/10.1016/S0011-9164(04)90013-6.
[67] M. Chen, T. Wu, K. Yang, W. Zhang, X. Wang, High flux and selectivity of poly(m-phenylene isophthalamide) loose nanofiltration membrane prepared by mussel-inspired co-deposition for dye/salt separation, Iran. Polym. J. 34 (2025) 703–713, https://doi.org/10.1007/s13726-024-01404-8.
[68] W. Xie, G. Chen, C. Chen, Z. Song, Q. Wu, L. Tian, Z. Dai, S. Liang, P. Tang, X. Zhang, J. Ma, B. Liu, Polydopamine/ polyethyleneimine/ MOF ternary-coated poly (vinyl chloride) nanocomposite membranes based on green solvent for shale gas wastewater treatment, J. Membr. Sci. 665 (2023) 121100, https://doi.org/10.1016/j.memsci.2022.121100.